Si/Fe flux ratio influence on growth and physical properties of polycrystalline β-$FeSi_2$ thin films grown on Si(100) surface

I.A. Tarasov[a,b]*, M. A. Visotin[b,c], A. S. Alexandrovsky[b], N.N. Kosyrev[b], I.A. Yakovlev[a,b], M.S. Molokeev[b,d], A.V. Lukyanenko[b,d], A.S. Krylov[b], A. S. Fedorov[b,d], S.N. Varnakov[a,b], S.G. Ovchinnikov[a,b].

[a]*Siberian State Aerospace University, 31 Krasnoyarsky Rabochiy Av., Krasnoyarsk 660014 Russia*
[b]*Kirensky Institute of Physics, Federal Research Center KSC SB RAS, Akademgorodok 50, bld. 38, Krasnoyarsk 660036, Russia*
[d]*Siberian Federal University, Institute of Engineering Physics and Radioelectronics, 660041, Krasnoyarsk, Russia*
[d]*Far Eastern State Transport University, Serysheva str. 47, Khabarovsk 680021, Russia*

ABSTRACT

This work investigates the Si/Fe flux ratio (2 and 0.34) influence on growth of β-$FeSi_2$ polycrystalline thin films on Si(100) substrate at 630 ˚C. Lattice deformation for the films obtained are confirmed by X-ray diffraction analysis (XRD). The volume unit cell deviation from that of β-$FeSi_2$ single crystal are 1.99 % and 1.1 % for Si/Fe = 2 and Si/Fe = 0.34, respectively. Absorption measurements show that the indirect transition (~ 0.813 eV) of the Si/Fe = 2 sample changes to the direct transition with a bandgap value of ~0.806 eV for the sample prepared at Si/Fe = 0.34. Along with this direct transition, the absorption spectra exhibit an additional feature with an excitation energy of ~0.56 eV. Surface magneto-optic Kerr effect (SMOKE) measurements detect ferromagnetic behavior of the β-$FeSi_2$ polycrystalline films grown at Si/Fe = 0.34 at T=10 K, but no ferromagnetism was observed in the samples grown at Si/Fe = 2. Theoretical calculations refute that the cell deformation can cause the emergence of magnetization and argue that the origin of the ferromagnetism, as well as the lower impurity direct transition, is β-$FeSi_2$ stoichiometry deviations. Raman spectroscopy measurements evidence that the film obtained at Si/Fe flux ratio equal to 0.34 has the better crystallinity than the Si/Fe = 2 sample.

Keywords: β-$FeSi_2$ iron disilicide; optical properties; reflection high-energy electron diffraction; Raman spectroscopy; ab initio calculation

1. Introduction

Iron silicides are under intensive investigations now due to their compatibility with silicon technology, economic benefits and abundance in the Earth crust [1]. The iron-silicon phase diagram contains several compounds where the semiconducting phase, silicide ß-$FeSi_2$, is being heavily investigated now for two main applications; as a material for light emitting diodes and as a thermoelectric material. Moreover, a direct band gap observed of 0.87 eV and large optical absorption coefficient ($\alpha>10^5$ cm^{-1}) is favorable for photovoltaic utilization. While bulk ß-$FeSi_2$ semiconductor exhibits paramagnetic properties, nanosized ß-$FeSi_2$ silicide shows a ferromagnetic behavior [2–5]. Such phenomenon is the subject of considerable interest since in such materials as magnetic semiconductors one may control and use spin-polarized current [6].

Thus, the extensive research on ß-$FeSi_2$ silicide thin film growth, which is being conducted by many research groups, focuses on finding mechanisms of controllable formation of desired physical properties. One of several approaches to cope with this task is the governing of lattice deformation. It was predicted that such a band-structure change as indirect to direct transition can appear due to ß-$FeSi_2$ thin film lattice stress [7]. On the other hand, the lattice deformation influence on direct transition energy was experimentally explored [8–10], which gave qualitative verification of earlier theoretical examinations. In these works, lattice deformation of ß-$FeSi_2$ thin films was induced by changing the Si/Fe flux ratio. The decreased ratios of Si/Fe = 0.5, 1.5 (relative to the nominal ß-$FeSi_2$ ratio, Si/Fe = 2) caused lattice constants deviation from those of the single crystal. Along with bandgap energy changes, the decreased ratios may result in the β-$FeSi_2$ stoichiometry deviation and changes in Fe-Si site occupation, which in turn could be reason for ferromagnetic ordering and appearance of the spin-polarization. In some application presence of the ferromagnetism in β-$FeSi_2$ is desirable, on the other hand this may diminish the other properties useful for industry applications, e.g. thermopower. Ferromagnetism in β-$FeSi_2$ will harm the thermoelectric performance due to additional spin fluctuation scattering, which is expected in the temperature range near the magnetic transition [6]. One may conclude, the Si/Fe flux ratio influence on physical properties of the ß-$FeSi_2$ thin films obtained remains unclear at the moment, although comprehensive knowledge of such processes could bring us considerable economic benefits.

In this report we make an attempt to shed light on the silicide thin film formation process at the different Si/Fe flux ratios (Si/Fe = 2, 0.34). We focus on stage-by-stage film growth consideration with the help of *in situ* methods, reflection high-energy electron diffraction (RHEED) and one-wave ellipsometry. Other *ex situ* methods, such as X-ray diffraction (XRD), atomic force microscopy (AFM), IR and Raman spectroscopy, spectral ellipsometry, magneto-optic Kerr effect (MOKE) and spectral magneto-ellipsometry, and Seebeck coefficient measurements were involved to clarify the matter of how the Si/Fe flux ratio affect physical properties of ß-$FeSi_2$ thin films grown on Si(100) substrates.

2. Experiment

The ß-$FeSi_2$ thin films were formed on 1˚- miscut vicinal p-Si(100) substrate (ρ ~ 5-10 Ωcm) at 630 ˚C by molecular beam epitaxy (MBE) in ultrahigh vacuum condition (UHV) in Angara chamber [11]. Prior to growth, Si substrate was chemically cleaned by the technique described [12]. Si substrate was exposed to gradual thermal treatment for 3 hours to 630 ˚C at rate of 4˚C/min in UHV (base pressure 6.5×10^{-8} Pa). In order to obtain an atomically clean silicon surface the wafer was flashed at 850-900 ˚C until well-ordered (2×1)

Corresponding author. Tel.: +7 391 249-45-56;
fax: +7 391 243-89-23.
E-mail address: tia@iph.krasn.ru (I.A. Tarasov)

reconstruction appeared in the RHEED. After the specimen was cooled down to 630 ˚C Fe and Si were deposited simultaneously with the growth rates of 0.1 and 0.34 nm/min during 180 min for sample S1, and 0.22 and 0.13 nm/min S2 during 240 min. The formation of the films structure along with RHEED was also controlled by an LEF-751M high-speed laser ellipsometer. The *ex situ* determination of the morphology, phase composition of the samples was performed by an AFM on Nanoink DPN 5000 and XRD methods on a D8 ADVANCE powder diffractometer (CuKα radiation, Ni filter) with a VANTEC linear detector. Raman spectra were acquired using a Horiba Jobin Yvon T64000 spectrometer in backscattering geometry at room temperature. The spectra were excited using an Ar+ laser (wavelength of 514 nm) with the power of 20 mW, corresponding to a laser power density of 60 W/cm^2. Optical bandgap energy of the films obtained were determined from the Tauc plots of spectra acquired by Shimadzu FTIR spectrometer in the wavelength range of 800 ÷ 3300 nm. Magneto-optic Kerr effect measurements were carried out in a wide temperature range (4 – 300 K) on NanoMOKE 2 system. Ellipsometric investigation were also performed using a variable spectroscopic ellipsometer Ellips-1801 at T = 296 K.

To investigate microscopic mechanisms that can alter electronic and magnetic structure, first-principle calculations were carried out. Density Functional Theory (DFT) within general gradient approximation (GGA) in PBE form (Perdew-Burke-Ernzerhof) [13] as implemented in VASP 5.3 (Vienna Ab-initio Simulation Package) [14,15] was used.

3. Results and discussion

3.1 Crystal structure characterization

The results of the sample XRD analysis are shown in Fig.1. All reflection peaks not belonging to Si(100) were successfully identified by orthorhombic phase β-$FeSi_2$ [16] in both samples. Moreover, according to the β-$FeSi_2$ powder intensities ratios, the larger intensity of the reflections close to 2θ = 46.14° reveals that the films are preferably oriented with the β(040) or β(331) planes on Si(100).

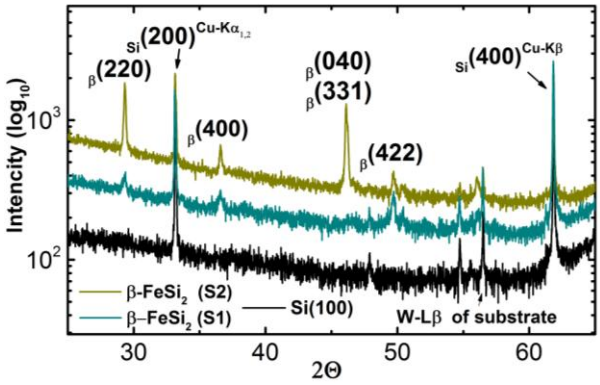

Fig. 1 X-ray diffraction pattern of ß-$FeSi_2$ thin films on Si(100) substrate; black curve depicts XRD pattern of film free Si(100) substrate, cyan curve corresponded to S1, yellow one – to S2.

Therefore, texture refinement was carried out in these two models. The refinements results are listed in Table 1. Based on the different XRD pattern and the reliability factors, in the case of the sample S1 it is difficult to precisely define which plane the texture is implemented on. However, the texture coefficient indicates that the preferable orientation is not strongly signified. While the XRD pattern for sample S2 reveals that the better model is the preferable orientation on β(331) plane. Thus the lattice constants deviation from those of the β-$FeSi_2$ single crystal [16] for Si/Fe = 2 are -1.69, +1.13, +2.59 % for *a*-,*b*-, *c*-axes, respectively, which resulted in the volume increment in ~ +0.7(5) %. In the case of the Si/Fe = 0.34 the constants of a-axis is shrunk by -2.22 and that of *b*-, *c*- axis is expanded by + 0.2 %, +3.18%. The volume expansion is ~ +1.1 (4) %. Thus, one can conclude that the influence of the Si/Fe flux ratio is hardly distinguishable within the confidence interval of the unit cell volume determination, whereas for the film texture it is crucial.

Table 1 XRD pattern refinement parameters of ß-$FeSi_2$ films crystal structure on the substrate Si (100) for two refinement models with different preferable orientation planes; the reliability factors show better values for the (331) model on case sample S2.

Model	(040) S1	(331) S1	(040) S2	(331) S2
Space group	*Cmca*	*Cmca*	*Cmca*	*Cmca*
a **, Å**	9.709(8)	9.71(1)	9.64(7)	9.658(5)
b**, Å**	7.801(5)	7.901(7)	7.863(5)	7.828(3)
c**, Å**	8.033(8)	8.03(1)	7.80(4)	8.076(9)
V**, Å^3**	608.4(9)	608(1)	591(5)	610.8(8)
Crystallites size, nm	29(2)	30(2)	44(1)	44(1)
Texture coefficient	0.81(3)	0.68(4)	0.24(1)	0.272(3)
R_{wp}**, %**	2.95	2.95	5.05	4.64
R_{exp}**, %**	2.10	2.10	2.20	2.20
R_P**, %**	2.04	2.04	3.16	2.13
R_B**, %**	3.76	3.38	7.64	4.39
χ^2	1.40	1.40	2.29	2.11

3.2 In situ characterization of the growth kinetics

Figure 2 represents the time evolution of the ellipsometric parameters ψ and Δ during the synthesis of the samples S1 and S2. To carry out preliminary analysis of the ψ, Δ time evolution the theoretical ψ, Δ dependencies on the growing film thickness with different complex refractive index were calculated. A simple growth model was used: a single solid isotropic layer on an isotropic substrate: λ = 632.8 nm, φ = 70˚, N_{sub} = 4.110-0.014*i*, N_a = 1, d_{film} = 70 nm, where N_{sub} - substrate complex index of refraction at T = 450˚ C, N_a – ambient refractive index, d_{film} - the final film thickness value. The following values of the refractive index and the extinction coefficient of the growing film were used: *n* = 3.79, *k* = 1.8, 2.4, 3.0, 3.6. The calculated ψ, Δ thickness dependencies indicate the evaluated optical parameters values are close to *n* = 3.79 и *k* = 2.10. Thus, we can conclude the β-$FeSi_2$ has formed and has optical constants, which are consistent with those of β-$FeSi_2$ compound in the literature available, *n* = 4.29, *k* = 2.84 at T = 23 °C [17].

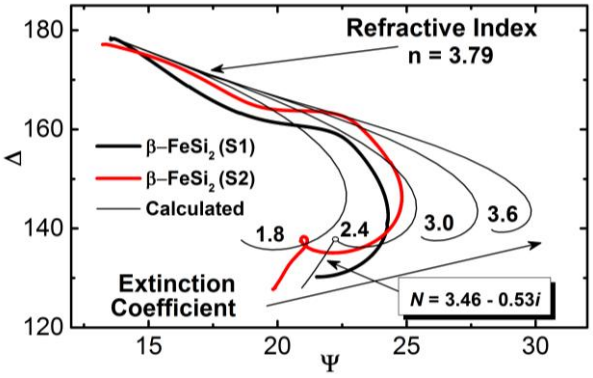

Fig. 2 Evolution of the ellipsometric parameters ψ and Δ obtained from real-time monitoring of the ß-$FeSi_2$ films. The thin black curves correspond to the calculated ψ - Δ dependencies for growing films with the refractive index and extinction coefficient indicated on the plot

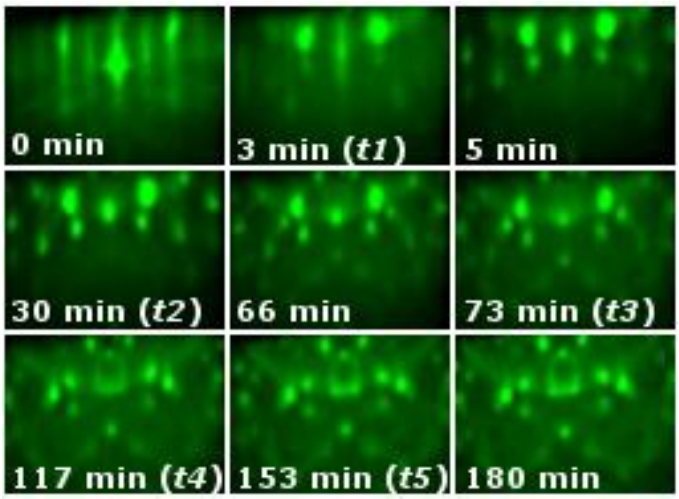

Fig. 4 The RHEED pattern time evolution during the growth of β-$FeSi_2$ film on Si(100) surface at 630 ˚C (sample S1). Notation in parentheses indicates the key time points of the optical parameters trajectory changes (Fig.5).

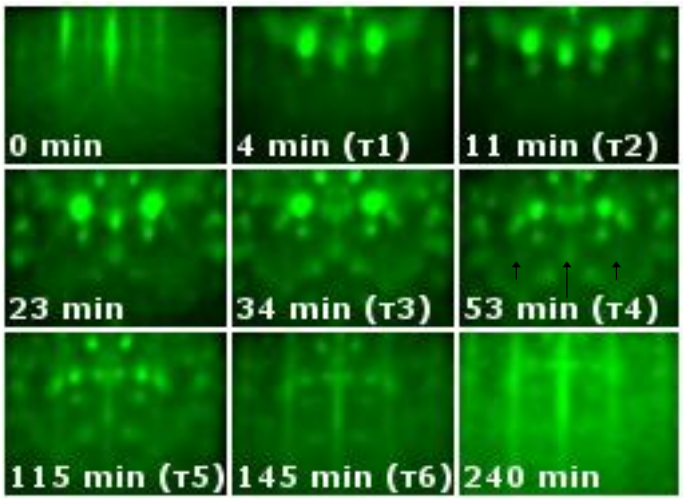

Fig. 6 The RHEED pattern time evolution during the growth of β-$FeSi_2$ film on Si(100) surface at 630 ˚C (sample S2). Notation in parentheses indicates the key time points of the optical parameters trajectory changes (Fig.5).

It should be noted that the ψ - Δ curve for sample S2, obtained under the Si/Fe flux ratio equal to 0.34, has a distinctive loop-like feature in the final stages of growth. This behavior is consistent with the formation of a layer which has a lower absorption value $k = 0.53$. We assume that at some point the surface roughness begins to increase and the effective optical parameters in this case correspond to similar refraction and absorption indices of the β-$FeSi_2$ islands and void mixture [18].

In order to acquire *n, k, d* time evolution profiles the quick ellipsometric technique for determining the thicknesses and optical constant profiles, which was developed by the authors earlier, [19] was utilized. The calculation results obtained are presented in Fig. 5. It can be seen that the *n* and *k* optical constants profiles for both samples have a similar behavior. Stabilization of change in the refractive indices and absorption takes place for these samples at $t = 150$ min. The value of the final film thickness β-$FeSi_2$ (S1) corresponds to $d = 55.5$ nm. For the sample S2 final film thickness cannot be determined, since the time $t = 220$ min (loop-like feature time point) thickness decrease is observed (not shown here). This behavior is not physical and may be related both to the processes when the thickness of the silicide film β-$FeSi_2$ reaches a value whereby light is not reflected from the substrate surface, as well as when the growth mode begins to be different from the optical model utilized.

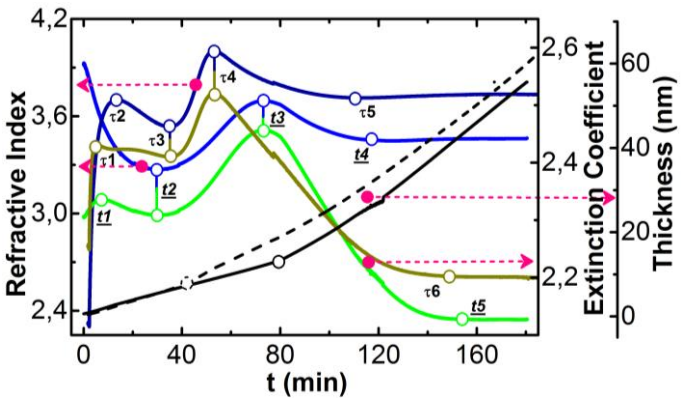

Fig. 5 The dependence of the refractive index, extinction coefficient and thickness growing β-$FeSi_2$ films on Fe, Si deposition time for sample number S1 (blue, green, solid black) and S2 (dark blue, dark yellow, dashed black) at wavelength is 632.8 nm; open circles on the curves depict the key time points of the change in parameter's trajectory. These time points correspond to those in RHEED patterns evolution, which is shown on Fig. 4,5

In both cases the calculation with the optical model "substrate - film - ambient" becomes invalid. The resultant complex refractive index values for the samples at time $t = 180$ min (S1 synthesis end time point) are $N_{S1} = 3.465\text{-}2.126i$, $N_{S2} = 3.735\text{-}2.2i$, which is also close to the the values for iron disilicide obtained by other authors, $n = 4.29$, $k = 2.84$ [17].

The refractive index profile (Fig. 5) for the sample S1 undergoes a trajectory change three times at the time points (t_2 = 30 minutes, t_3 = 73 min, t_4 = 117 min), and the absorption profile - four times (t_1 = 5 min, t_2 = 30 min, t_3 = 73 min, t_5 = 153 min). These key time points are depicted by open circles on the curves for easier correlation with RHEED patterns (Fig.4, 6). In turn, the profiles of the optical constants for the sample S2 have six distinctive changes in their trajectory at time points ($\tau_2 = 11$, $\tau_3 = 34$, $\tau_4 = 50$, $\tau_5 = 105$ min) for *n* and ($\tau_1 = 4$, $\tau_3 = 34$, $\tau_4 = 50$, $\tau_6 = 145$ min) for *k*. In comparison with the sample S1 n k trajectory changes for S2 occur at earlier time points. This could be caused by both a slight difference in the quantity of atoms coming to the surface or an inherent growth process.

It is difficult to precisely interpret the appearance of the profiles since this requires sophisticated approaches and further examination. However, it should be said that the profiles of the optical constants reflect a combination of many processes taking place during the film growth; changes in the morphological and structural properties of the films, their chemical composition and the temperature. The end of a certain stage, for example, the chemical composition evolution, and the beginning of another stage may not coincide with the onset of changes, for example, in the film morphology. Thus, the change of the trajectory curves of effective *n* and *k* may indicate that the impact of one process begins to dominate over the other. With a simple qualitative estimation of the profiles this tool might be useful for quick indication of the nanostructures growth complexity. For instance, the growth of polycrystalline Ni films on glass [20] or the growth of the epitaxial and polycrystalline Fe_3Si films on silicon have only two segments on the *n*, *k* profiles [11], whereas the synthesis of the β-$FeSi_2$ films on Si(100) surface at 630 ˚C demonstrates a variety of the growth stages.

To compare the features observed in *n* and *k* profiles with changes in the structural properties and morphology of the growing film surface electron diffraction patterns were extracted at indicative time points (***t*** = 3, 30, 73, 117, 153 min – Fig. 4, S1), (**τ** = 4, 11, 23, 32, 53, 115, 145, 240 min – Fig. 6, S2) for both samples. The images of the diffraction patterns at *t*

= 0 min (Fig. 4,6) correspond to the Si(100) 2x1 surface reconstruction. Comparing RHEED patterns received in the time interval t = 3($\mathbf{t_1}$) – 30($\mathbf{t_2}$) min for S1, and in t = 4($\boldsymbol{\tau_1}$) – 11($\boldsymbol{\tau_2}$) min for S2 with the patterns calculated in works [21,22], we can conclude that the α-$FeSi_2$ and γ-$FeSi_2$ phases form during these time periods. This pattern persists up to the time point $\boldsymbol{t_2}$ = 30 min (Fig. 4, S1), t ≈ 20 min (Fig. 6, S2) when additional reflections become visible, which characterizes the beginning of the changes in the structural properties of the film. At time t = 66 min RHEED image (Fig. 4, S1) is characterized by a plurality of transmission diffraction reflections formed by three-dimensional single-crystal islands of the $FeSi_2$ silicides, as in the case of the sample S2, where similar reflections occur at t = 23 – 34($\boldsymbol{\tau_3}$) min. By the time $\boldsymbol{t_3}$ = 73 min (the sample S1) additional reflections, whose intensity increases up to $\boldsymbol{t_4}$ = 117 min, appear, and the intensity of the reflections appeared in the earlier growth stages, which characterize the α-$FeSi_2$ and γ-$FeSi_2$ silicide formation, decreases by slow transformation into reflections located at different reciprocal space coordinates. As can be seen from the diffraction pattern at $\boldsymbol{t_5}$ = 153 min no new reflections occur but the reflections which appeared at $\boldsymbol{t_3}$ = 73 min have greater intensity. Further, the diffraction pattern does not change until the growth ends (t = 180 min). The final RHEED pattern can be understood as the surface consisting of single crystal β-$FeSi_2$ islands with multiple orientations relative to the $[-110]_{Si}$ direction. In turn, for the sample S2 by the time $\boldsymbol{\tau_4}$ = 53 min subtle streak-like reflections appear (indicated by arrows). These reflections may be explained by formation of a surface consisting of single crystal islands, whose height is substantially less than the width. The diffraction patterns at t = 115($\boldsymbol{\tau_5}$) min and t = 145($\boldsymbol{\tau_6}$) min show that the intensity of the streaks increases, this indicates that β-$FeSi_2$ monocrystalline islands increase in surface area relative to the three-dimensional single-crystal islands.

These results are also confirmed by XRD modeling, where the sample S1 texture coefficient on β(331) is 0.68(4), whereas for the sample S2 it is 2.5 times less, 0.272(3). Thus, the presence of both large β-$FeSi_2$ flat islands, equally oriented to the Si(100) plane and aligned in the same direction, as well as smaller ones, oriented on a set of planes, should be expected. Additionally, the AFM image (Fig. 7b) reveals the presence of such large flat islands on the sample S2 surface with typical sizes of 800x800x140 nm enclosed within the small ones. In turn, the AFM of the sample S1 surface does not display any islands with such width value. Typical island size is 100x100x20 nm. Therefore, the films obtained are not assumed to be continuous and represent nanostructures composed of iron disilicide clusters with different density and average size [23]. The higher density and smaller cluster sizes correspond to the sample S1.

Thus, one may conclude that the behavior of the optical parameters as a whole reflects the changes of the morphology and structural properties of the growing β-$FeSi_2$ films. The n k trajectory bends corresponding to the change in the surface condition are arranged in the earlier time periods for such profiles of the sample S1. This is consistent with the evolution of the corresponding RHEED patterns, where a variety of the changes in the structural properties and the morphology of the sample S2 also occur earlier than in S1.

Five main growth stages can be distinguished by qualitative estimation of the RHEED and n, k profiles evolution for both β-$FeSi_2$ growing films at different Si/Fe flux ratios. The first corresponds to the initiation of the α-$FeSi_2$ and γ-$FeSi_2$ oriented islands growth [21,22] ($\boldsymbol{t_{start}}$ – $\boldsymbol{t_1}$ S1, $\boldsymbol{\tau_{start}}$ - $\boldsymbol{\tau_1}$,$\boldsymbol{\tau_2}$ S2). The second ($\boldsymbol{t_1}$ – $\boldsymbol{t_2}$ S1, $\boldsymbol{\tau_1}$,$\boldsymbol{\tau_2}$ – $\boldsymbol{\tau_3}$ S2) is the continuation of growth with appearance of new silicide islands orientation. The third

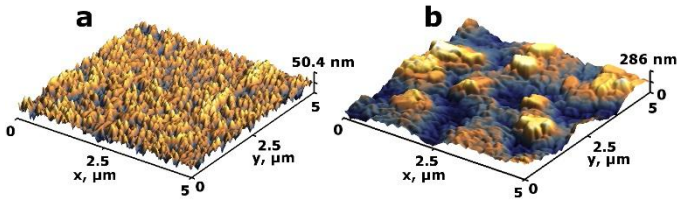

Fig. 7 AFM images for samples a) S1, average film surface roughness R_a = 5.2 nm and average maximum roughness height R_{tm} = 27.1 nm, the maximum profile valley depth R_v = 24.19 nm b) S2, average film surface roughness R_a = 43.3 nm and average maximum roughness height R_{tm} = 131.2 nm, the maximum profile valley depth R_v = 111.2 nm typical size of higher flat islands is 800x800x140 nm

($\boldsymbol{t_2}$ – $\boldsymbol{t_3}$ S1, $\boldsymbol{\tau_3}$ – $\boldsymbol{\tau_4}$ S2) corresponds to the smooth transition from the previous step to the formation of monocrystalline β-$FeSi_2$ three-dimensional islands with different orientations on diminishing α-$FeSi_2$ and γ-$FeSi_2$ islands growth. The fourth ($\boldsymbol{t_2}$ – $\boldsymbol{t_3}$ S1, $\boldsymbol{\tau_3}$ – $\boldsymbol{\tau_4}$ S2) is characterized by the increase in roughness for both samples until the final fifth stage ($\boldsymbol{t_4}$, $\boldsymbol{t_5}$ – $\boldsymbol{t_{fin}}$ S1, $\boldsymbol{\tau_4}$, $\boldsymbol{\tau_6}$ – $\boldsymbol{\tau_{fin}}$ S2), which is characterized by non-changing RHEED pattern and non-changing n, k values.

Even though the behavior of the profiles during the fourth stage ($\boldsymbol{t_3}$ – $\boldsymbol{t_3}$, $\boldsymbol{t_5}$ S1, $\boldsymbol{\tau_4}$ – $\boldsymbol{\tau_4}$, $\boldsymbol{\tau_6}$ S2) is similar in both samples, when the corresponding RHEED patterns are already not in accordance. The kinks in the thickness at t ≈ 80 min, S1 and t ≈ 40 min, S2 (Fig. 5) indicate an increase in the growth rate, which may be evidence for this behavior in the growth kinetics. The switch from the formation of α-$FeSi_2$ and γ-$FeSi_2$ islands to the β-$FeSi_2$ ones, in the case of the S1, continues with no strong change in the roughness, whereas for S2 there is a noticeable increase in roughness (Fig.7). In particular, the higher roughness value for the sample S2 results in increased thicknesses (Fig. 5), although during earlier stages the thicknesses for both samples are virtually the same.

3.3 Growth kinetics discussion

At the decreased Si/Fe flux value (0.34 corresponding to the stoichiometry of the Fe_3Si phase) Si atoms, due to the thermal diffusion from substrate, accomplish $FeSi_2$ stoichiometry. The reaction is exothermic and the heat outcome can be estimated as in [24] using the data from [25]. The estimated heat of β-$FeSi_2$ is 25.2 kJ per mole of deposited iron atoms.

The energy realized can increase the temperature substrate surface over 630 °C, which in turn could result in decrease of the stable clusters surface density with the average cluster size increase, that we have observed in our experiments (Fig.7). Since single-atom diffusion is assumed to be the most predominant contribution in during the growth and surface diffusion of clusters has a larger activation energy [27]. Thus, with slight temperature increase single atoms get more mobile on the surface and can diffuse over longer distances to stable clusters [26]. In the growth beginning initial precipitates of the α- γ-$FeSi_2$ form in the substrate due to lower surface energy and smaller value of the lattice misfit with silicon in comparison with β-$FeSi_2$. Further large precipitates grow at the expense of the small ones at both sides because of the Ostwald ripening [28,29]. Since, the changes in the ratio of width to height implies a minimization of the surface and interface energy. At some time point of the growth the α- γ-$FeSi_2$ islands reach some critical size and these new conditions, along with the lattice strain relaxation in the top layers in comparison with bottom ones strained by Si interface resulting in the better misfit value between α- and β-phases, make them to have energetically favorable shape, so that the surface energy alter and β-$FeSi_2$ phase nucleation becomes beneficial. It should be

noted that overall picture of the atom diffusion processes is not clear at the moment for this complex system and needs further examination.

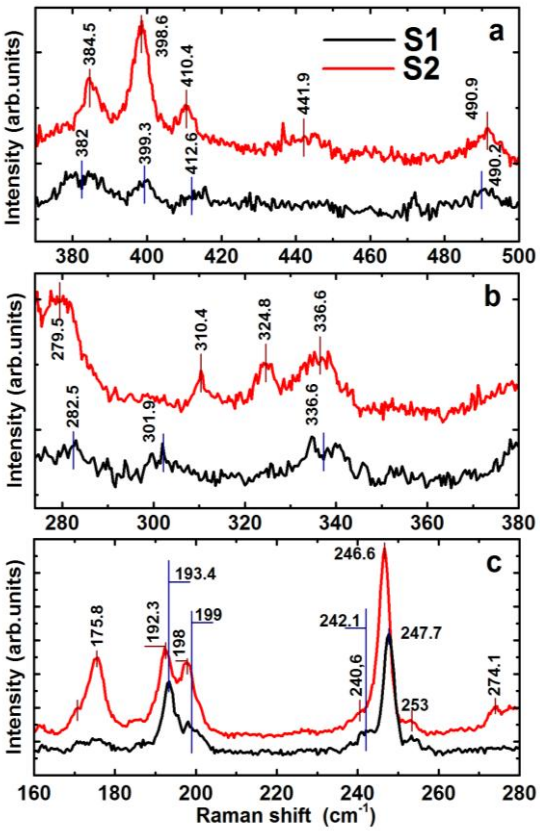

Fig. 10 The Raman spectra for the polycrystalline β-$FeSi_2$ thin films grown on Si(100) at 630 ˚C. Black line corresponds to the sample S1 and red line – S2.

3.4 Raman spectroscopy

The electronic structure near band-gap is very sensitive to lattice distortions and presence of the defects structural and chemical order. In turn, Raman spectroscopy is a very effective tool to investigate such changes in the materials. Despite the fact that we were not able to precisely detect lattice deformation from the XRD we expect to observe on Raman spectra features resulted from the lattice deformation and defects in occupancies of the Fe-Si sites.

The group factor analysis of orthorhombic lattice predicted 36 Raman active lines including 24 external modes and 12 internal modes. Raman peaks located in the range between 180 and 280 cm^{-1} are caused only by iron displacements. The vibrational features of both iron and silicon atom displacements are dominant in 280-380 cm^{-1} and whereas only that of silicon displacements exist above ~400 cm^{-1} [30–32].

Comparing spectra for the S2 film on Si(100) to the S1 one as seen in Figure 10, the Raman peaks increase slightly in intensity and most of them undergo a red shift due to the lattice deformation [30]. The main 246.6 cm^{-1} (S2) peak attributed to A_g-mode is shifted toward lower energies regarding to 247.7 cm^{-1} (S1) thereby indicating stronger lattice deformation of the sample S2. The lattice stress decreases the bond-length, thereby diminishing the oscillator strength of the Fe–Si bonds, which leads to the red shift. Terai et al. showed [8,30] that in the epitaxial β-$FeSi_2$(100)//Si(001) films $\Delta a/a_{bulk}$ value varies from 0.15 up to 0.28 % with increasing annealing temperature (600 – 900℃), whereas the distinctive Raman line decreased from 248.8 cm^{-1} to 247.9 cm^{-1} – 0.9 cm^{-1} corresponding to the change $\Delta a/a_{bulk}$ of 0.13 %. The $\Delta(b,c)/(b,c)_{bulk}$ was expanded from +0.05 to +0.19 (0.14 % increase). The same Raman line observed inpolycrystalline β-$FeSi_2$ film at room temperature is ~247.8 cm^{-1} [30], which is in the good agreement with the value obtained on the strongly disordered sample S1 (247.7 cm^{-1}). Consequently, we can conclude that the further shift of the distinctive Raman line to 246.6 cm^{-1} (S2) results from the strong texture on (331) plane. Such single-crystal clusters oriented parallel to Si(100) plane undergo the high lattice deformation, according XRD $\Delta a/a_{bulk}$ = -2.22 %, $\Delta(b)/(b)_{bulk}$ = +0.2 % and $\Delta(c)/(c)_{bulk}$ +3.18 %. The FWHM values for both samples are comparable to the values reported for β-$FeSi_2$ bulk crystals [32].

Weak Raman lines located at ~240.6 and 253 cm^{-1} have not been observed yet in β-$FeSi_2$ single crystals [32,33]. It is reported that the peak at 240.6 cm^{-1} as shown Fig.10(c) may be due to Si vacancies at the nanocluster interfacial regions [34] so that disorder-induced Raman scattering appears. This assumption is confirmed by increased intensities of this Raman line corresponding to the sample S1, where the interface region playa an important role since the portion of interfacial area is higher in S1 due to smaller cluster size (Fig. 7). Furthermore, the other important feature on the S1 Raman spectra, as has already mentioned is the absence of some scattering lines. The intensity of the Raman lines 175.8 (B_{2g}, B_{3g}), 198 cm^{-1}(unknown) (S2), produced by only iron displacements, are strongly reduced in the sample S1. Such behavior along with weaker and broader lines in Fig.10(b) and Fig. 10(a) (S1), where above 400 cm^{-1} only Si atoms displacement is responsible, could be evidence for strong disorder in the positions of Si atoms. Since the sample S1 was prepared under the Fe/Si flux ratio equal to 2, i.e. with proper stoichiometry value, additional Si atoms arriving from the substrate due to thermal diffusion from at 630 ˚C could alter the stoichiometry of the disilicide film to higher Si content. Therefore, the silicon atom could occupy the Fe site or interstitial sites in the orthorhombic β-$FeSi_2$ unit cell leading to modification of the electronic structure.

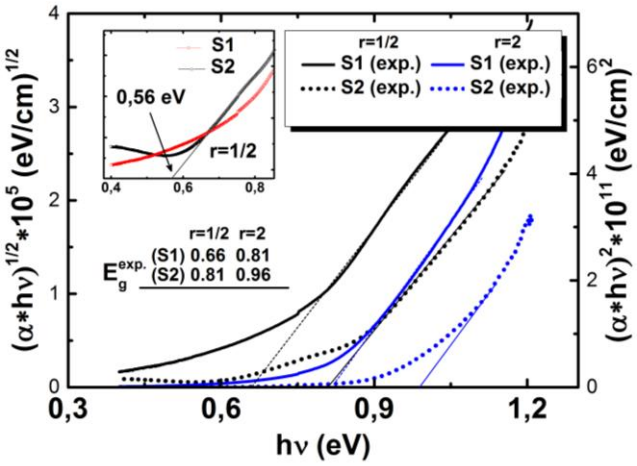

Fig. 8 $(\alpha \times h\nu)^{1/2}$ and $(\alpha \times h\nu)^2$ versus $h\nu$ plots for β-$FeSi_2$ films (grown by MBE at 630 °C on Si(100)) measured at 300 K; α is the absorption coefficient and $h\nu$ is the photon energy.

3.5 Optical properties

Reduction of the direct bandgap in β-$FeSi_2$ thin film by up to -0.2 eV with cell shrinking was reported earlier [8–10]. The direct transition energy was shifted to lower values, which has also been confirmed by theoretical calculation [7]. However, the information about the bandgap nature and its energy shift under larger unit cell volume reduction or expansion in comparison with the lattice parameters reported earlier [8–10,17], to the best of our knowledge, is not currently available. Thus, Figure 8 represents Tauc plot for allowed direct (r = ½) and indirect (r = 2) transitions for both samples (S1 and S2).

Therefore, evaluating linear regions on the Tauc plot curves for both samples we conclude that the sample S2 has a direct bandgap with the transition energy of ~0.81 eV, which is in good agreement with the experimental data on β-$FeSi_2$ films bandgap values [9,35]. Along with the main direct transition $E_g^{(main)}$ ~0.81eV the other one with the energy of 0.56 eV could be determined (see inset in Fig. 8). Such a smaller transition could result from the impurity level. This could be caused by several factors; off-stoichiometry, changes in Fe-Si site occupation in the β-$FeSi_2$ crystal structure, defects and surface electron states in the grain boundaries of the polycrystalline film. At the lower energies one can clearly see an increase in absorbance in the range of 0.4 – 0.56. Such behavior is simply explained with the degenerate nature of the semiconductor. The Fermi level is partly located in the valence band so that the low energy transitions can take place from the electron states beneath the Fermi level to the unoccupied states in the valence band maximum (VBM). Conversely, the behavior of the Tauc plot for the sample S1 is better described by indirect transition with almost the same energy, ~ 0.81 eV.

Migas et al. showed earlier that the change from indirect to direct bandgap may take place in highly anisotropically strained β-$FeSi_2$: in one case the lattice deviations were $\Delta a/a_{bulk}$ = +7.32 %, $\Delta(b)/(b)_{bulk}$ = -1.7 % and $\Delta(c)/(c)_{bulk}$ = +2.69 %; in another case - $\Delta(c)/(c)_{bulk} \leq$ -4 %. However, the magnitudes of deformation were greater than in S1 and S2. To check whether the features in absorption spectra observed in disilicide thin films grown at different co-deposition stoichiometry, electronic structures appear due to deformation in the β-$FeSi_2$ unit cells, DFT calculations were carried out. First of all, an undeformed cell was fully optimized without any constraints on the lattice constants. The resulting cell sizes (9.861, 7.762 and 7.807 Å) agree well with known single-crystal experiments. The bandgap was indirect with the width of 0.671 eV, while the lowest direct transition was 0.721 eV. Then, two deformed cells with lattice parameters constrained to the corresponding XRD data for the samples S1 and S2 were calculated. Both cells also had indirect bandgaps. In the case of the cell deformed as in the sample S1, the bandgap and the lowest direct transition were 0.613 and 0.726 eV respectively. In the case of the cell corresponding to S2, the values were 0.628 and 0.774 eV, respectively. Despite underestimating the absolute values, the DFT calculations evidence that the lattice deformations of the samples S1 and S2 are insufficient to cause the change from indirect to direct bandgap.

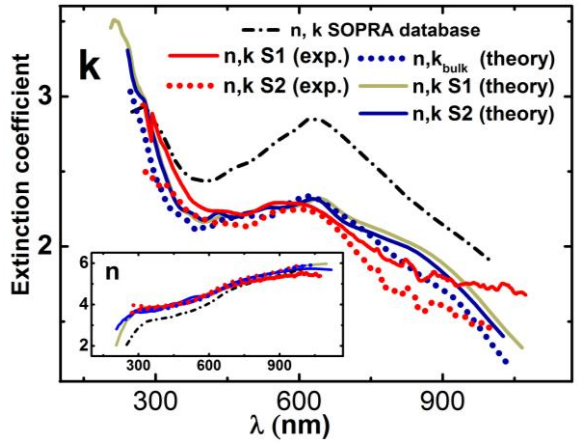

Fig. 9 Extinction coefficient spectra (refractive index spectra are shown in inset) obtained by ab initio calculation for the deformed unit cells (undeformed bulk – blue dotted, S1 – yellow, S2 – blue) and the spectra extracted from the ellipsometric measurements modelling (S1 – red solid, S2 – red dotted); black dash-dotted curve depicts the spectra from the SOPRA database [http://sspectra.com/sopra.html; inset reflects refractive index spectra for the same legend accordance

In addition to the absorption edge examination of the polycrystalline β-$FeSi_2$ films (S1 and S2) grown on Si(100) at 630 ˚C we also made an attempt to display peculiarities in the appearance of their refractive index and extinction coefficient spectra in the range 250 – 1000 nm by means of modelling ellipsometric spectra. It is clear that the β-$FeSi_2$/Si(100) resultant system is very complicated to carry out precise estimation of the *n*, *k* and thickness of the film using the ellipsometry method. The typical crystallite size (Fig. 7) is comparable with the probing radiation wavelength, which makes the utilization of the effective medium approximation [18] inappropriate in some wavelength ranges. Nevertheless, the following procedures were applied to characterize the ellipsometrical measurements.

Since the *n*, *k ab initio* calculated spectra for deformed unit cells S1 and S2 do not differ greatly from each other we used only the S1 *ab initio* calculated spectra to fit the experimental ellipsometric data for two samples, S1 and S2. Optical model applied was three solid isotropic layers on the silicon substrate, namely, roughness layer (RL), β-$FeSi_2$ silicide layer (SL) and transition β-$FeSi_2$ –Si layer (TL). Effective layer contains three components: void, silicon dioxide, β-$FeSi_2$. The effective *n*, *k* parameters were calculated according Bruggeman effective medium approximation [18]. As it is known that β-$FeSi_2$ phase are subjected to air oxidation with SiO_2 formation [], that is why we included the silicon dioxide component to the roughness layer. Transition layer is two component layer (Si and β-$FeSi_2$) with the volume fraction q = 0.5 for both. The fitted values were thicknesses of the RL, SL, TL layers and two volume fraction values for β-$FeSi_2$ and SiO_2, q_1, q_2, respectively. The fitting range q_1, q_2 parameters were framed according to the AFM images analysis for both samples. The range was 0.5-0.9 for q_1, and 0.01-0.3 for q_2. Consequently, fitting error function [36] for S1 was ~ 0.37, for the sample S2 ~ 0.81. The following fitted parameters values were extracted; (S1) → thickness of the transition layer is 12.6 nm, the thickness silicide layer is 25.9 nm, thickness of the roughness layer is 10.9 nm, the silicide volume fraction is 0.66, the SiO_2 volume fraction is 0.28, the void volume fraction is 0.06; (S2) → thickness of the transition layer is 95.2 nm, the thickness silicide layer is 79 nm, thickness of the roughness layer is 19.5 nm, the silicide volume fraction is 0.64, the SiO_2 volume fraction is 0.18, the void volume fraction is 0.18. Thus, the fitted parameters are in approximate agreement with the AFM analysis results (Fig. 7) of the β-$FeSi_2$/Si(100) film systems. Further, having obtained the parameters values we completed a reverse ellipsometrical data processing – using these parameters derived the *n*, *k* spectral dependencies were calculated so that one can conclude about the discrepancy behavior between *ab initio* calculated and experimental spectra.

The experimental spectra of the refractive index and extinction coefficient reflect the overall wavelength range behavior of such spectra for the β-$FeSi_2$ bulk crystal (SOPRA database curve). The discrepancy between the S2 experimental curve of the extinction coefficient and the theoretical one becomes larger in the infrared and ultraviolet regions, whereas the refractive index does not undergo strong noticeable changes over the whole wavelength range (Fig. 9 inset). . This could indicate that the extinction coefficient in near infrared region is more sensitive to lattice volume reduction. Thus, the effect of lattice expansion or reduction on optical parameters of β-$FeSi_2$ needs to be clarified in further examination.

3.6 Magneto-optical Kerr effect measurements

In order to examine magnetic properties of the samples obtained, temperature-dependent magneto-optic measurements in longitudinal geometry have been performed at a photon energy of 2 eV. Figure 11 represent the result of the measurements at 4 K for the sample S1 and at 10 K for the sample S2. One can notice an appearance of the small hysteresis observed on the right panel (S2), whereas no MOKE signal was detected on the sample S1. It can be clearly seen that the value of the applied magnetic field is not enough to saturate the magnetization of the sample S2 completely. Moreover, this weak ferromagnetism disappears at temperatures higher than 100 K, which is in good agreement with other evidences obtained earlier [4].

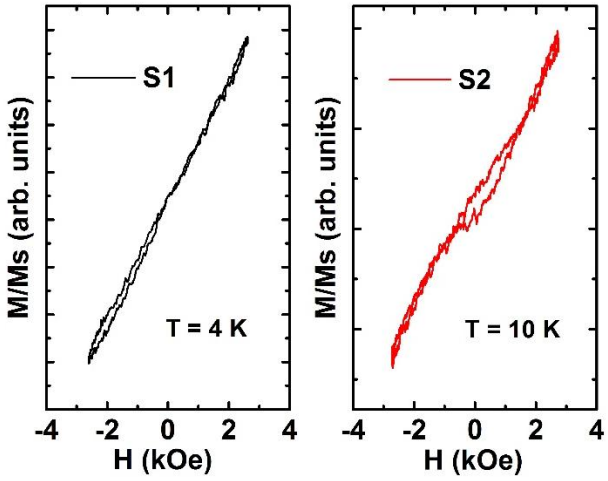

Fig. 11 MOKE hysteresis measurements for the β-$FeSi_2$ film grown at Si/Fe flux ratio equal to 2 (left panel) and 0.34 (right panel) on Si(100) surface at 630 ˚C.

It can be concluded that one of the reasons for ferromagnetic behavior of the β-$FeSi_2$ film/silicon substrate system is the existence of the ferromagnetic interface consisting of Fe-rich alloys between the β-$FeSi_2$ film and substrate [2,3]. However, this statement is not appropriate in our case because no reflections corresponding to ferromagnetic Fe-rich silicides, which are usually formed in B2 crystal structure [37], appeared on RHEED pattern. Another reason for the ferromagnetism, and mentioned in the literature, that it may be caused by the presence of so-called ferromagnetic impurity aggregates [4,38], which could be β-$FeSi_2$ clusters or sublayer with stoichiometry deviation and changes in Fe-Si site occupation or ferromagnetic α-$FeSi_2$ phase clusters [39]. One way or another in such systems local moments exist on impurity atoms or in some cases at other point defects. Those moments are then coupled through the host lattice, typically mediated by conduction electrons [6]. According to the two-valence-band model [4], such impurities create additional impurity level in the forbidden band, which is located at some distance from the upper edge of the iron valence band. At very low temperature, the Fermi level E_F lies between the upper edges of the 3d´ and 3p valence band the 3d´ band (Fig. 12) therefore it contributes mainly to the conduction. The carriers are moving among the iron atoms resulting in a low mobility due to magnetic interaction and scattering from the magnetic iron atoms, which become apparent in transport properties, anomalous Hall coefficient and resistivity temperature dependencies [4,38]. In turn, the impact of the interband electronic transitions from the 3d´ band to the conductance band at low temperatures becomes determinant for magneto--optical activity, since the intensity of interband electronic

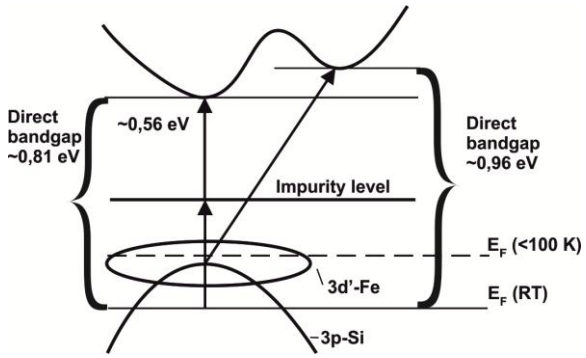

Fig. 12 Schematically depicted near bandgap structure illustrating two valence-band model. Energy of the transitions are extracted from transmitivity measurements

transitions from occupied states of spin-down and spin-up subzones of the impurity atoms with non-zero magnetic moment, to vacant states is different for light with linear polarization. When the temperature is increased, the Fermi level shifts from the spin-polarized iron 3d electrons band into the non-polarized silicon 3p band, which results in the Kerr effect disappearing.

According to the direct transitions energy, determined earlier, the value of the impurity level (Fig. 12) should locate at 0.25 eV above the Fermi level ($E_g^{(main)}$ - $E_g^{(impurity}$). The increase of the absorbance, which is observed in the range of 0.55 – 0.4 eV, should correspond to low energy 3p→3p intraband and 3p→3d' interband transitions from the electron states beneath the Fermi level to the states above the Fermi level within valence band.

In our *ab initio* calculations, none of three β-$FeSi_2$ unit cells (two cells deformed as in the samples S1 and S2 and one undeformed, see 3.4) exhibit magnetic behavior. However, while S2 was grown at Fe-rich conditions (Si/Fe = 0.34), one may expect it to contain a lot of defects such as the Fe interstitials or silicon atom substitution by Fe. Our estimative calculations show that placing an interstitial iron atom in the center of orthorhombic pore result in cell magnetization of approx. 2 μB, with net magnetic moment on the defect atom of 1.25 μB. The substitutional defects cause higher cell magnetization of 4 μB, with net magnetic moment on the defect atom of 2.5 μB. It should be noted that Fe atoms in the vicinity of the defect obtain magnetic moments up to 0.5 μB, which indicates short-range magnetic ordering. Thus it can be speculated that Fe interstitials and the substitutional defects can be the origin of weak ferromagnetism in S2.

4. Conclusions.

To summarize, we have examined the growth kinetics, formation of the optical and magnetic properties and vibrational atom characteristics of β-$FeSi_2$ films grown on Si(001) at two very distinctive Si/Fe flux ratios (2 and 0.34), where 0.34 corresponds to the stoichiometry of the Fe_3Si silicide. The XRD and Raman spectra studies confirm that β-$FeSi_2$ thin film obtained at Si/Fe flux ratio equal to 0.34 has the better crystallinity than the Si/Fe = 2 sample. The growth kinetics is not the same in both cases. We suppose that under Fe-Si enriched flux additional energy is released in comparison with the case when the Si/Fe flux ratio = 2. The total quantity of the Fe and Si atoms participating in the chemical reaction on the silicide formation becomes larger due to arriving additional silicon atoms, which locally warms-up the sample surface, resulting in the surface energy change so that a new orientation of the β-$FeSi_2$ phase becomes possible. However, further

examination needs to be carried out to have a closer look at this issue.

We have found ferromagnetic ordering by magneto-optical Kerr measurements below 100 K in the β-$FeSi_2$ polycrystalline thin film prepared under the Fe/Si flux equal to 0.34. The ferromagnetism can be explained by the two valence-band model. According to the absorption measurements the impurity level is located 0.25 eV above the Fermi level. Preliminary *ab initio* calculations of Fe-enriched β-$Fe_{1+x}Si_{2-x}$ compounds evidence that Fe defects can induce ferromagnetism in thin films.

Thus, it has been shown that the change of the Fe/Si flux ratio can affect the lattice strain in the polycrystalline β-$FeSi_2$, through growth kinetics, which in turn modifies the band structure. The Fe/Si flux ratio changes do not result in proportional changes in the Fe or Si content of the β-$FeSi_2$ films obtained due to the thermal diffusion of the Si atoms from the substrate. However, the growth mechanisms responsible for appearance of the structural and chemical order defects caused by the off-stoichiometry (occupation of the Si atom sites by the Fe atoms and vice versa, presence of the Fe and Si atoms in the interstitial sites) along with their influence on the optical, magnetic and electronic properties of β-$FeSi_2$ compound are not fully understood at the moment and need to be further clarified.

Acknowledgments

This work was supported by the Russian Science Foundation, project no. 16-13-00060

References

[1] R. Amatya, R.J. Ram, Trend for thermoelectric materials and their earth abundance, J. Electron. Mater. 41 (2012) 1011–1019. doi:10.1007/s11664-011-1839-y.

[2] A.N. Hattori, K. Hattori, H. Daimon, β-$FeSi_2$ thin film grown on a Si(111) surface with ferromagnetic interface, J. Phys. Conf. Ser. 61 (2007) 404–408. doi:10.1088/1742-6596/61/1/081.

[3] A.N. Hattori, K. Hattori, K. Kodama, N. Hosoito, H. Daimon, Formation of ferromagnetic interface between β-$FeSi_2$ and Si(111) substrate, Appl. Phys. Lett. 91 (2007) 201916. doi:10.1063/1.2804006.

[4] O. Valassiades, C.A. Dimitriadis, J.H. Werner, Galvanomagnetic behavior of semiconducting FeSi2 films, J. Appl. Phys. 70 (1991) 890. doi:10.1063/1.349619.

[5] Z. He, S. Xiong, S. Wu, X. Zhu, M. Meng, X. Wu, Strong Facet-Induced and Light-Controlled Room-Temperature Ferromagnetism in Semiconducting b-FeSi2 Nanocubes, J. Am. Chem. Soc. 137 (2015) 11419–11424. doi:10.1021/jacs.5b06507.

[6] D.J. Singh, D. Parker, Itinerant magnetism in doped semiconducting β-$FeSi_2$ and $CrSi_2$, Sci. Rep. 3 (2013) 3517. doi:10.1038/srep03517.

[7] D.B. Migas, L. Miglio, Band-gap modifications of β−$FeSi_2$ with lattice distortions corresponding to the epitaxial relationships, Phys. Rev. B. 62 (2000) 11063–11070. doi:10.1103/PhysRevB.62.11063.

[8] K. Noda, Y. Terai, S. Hashimoto, K. Yoneda, Y. Fujiwara, Modifications of direct transition energies in β-$FeSi_2$ epitaxial films grown by molecular beam epitaxy, Appl. Phys. Lett. 94 (2009) 10–13. doi:10.1063/1.3155204.

[9] K. Noda, Y. Terai, N. Miura, H. Udono, Y. Fujiwara, Growth condition dependence of direct bandgap in β-$FeSi_2$ epitaxial films grown by molecular beam epitaxy, Phys. Procedia. 23 (2012) 5–8. doi:10.1016/j.phpro.2012.01.002.

[10] Y. Terai, K. Noda, K. Yoneda, H. Udono, Y. Maeda, Y. Fujiwara, Bandgap modifications by lattice deformations in β-$FeSi_2$ epitaxial films, Thin Solid Films. 519 (2011) 8468–8472. doi:10.1016/j.tsf.2011.05.021.

[11] I. a. Tarasov, Z.I. Popov, S.N. Varnakov, M.S. Molokeev, A.S. Fedorov, I. a. Yakovlev, et al., Optical characteristics of an epitaxial Fe_3Si/Si(111) iron silicide film, JETP Lett. 99 (2014) 565–569. doi:10.1134/S0021364014100105.

[12] I.A. Yakovlev, S.N. Varnakov, B.A. Belyaev, S.M. Zharkov, M.S. Molokeev, I.A. Tarasov, et al., Study of the structural and magnetic characteristics of epitaxial Fe_3Si/Si(111) films, JETP Lett. 99 (2014) 527–530. doi:10.1134/S0021364014090124.

[13] J.P. Perdew, K. Burke, M. Ernzerhof, Generalized Gradient Approximation Made Simple, Phys. Rev. Lett. 77 (1996) 3865–3868. doi:10.1103/PhysRevLett.77.3865.

[14] G. Kresse, J. Hafner, Ab initio molecular dynamics for liquid metals, Phys. Rev. B. 47 (1993) 558–561. doi:10.1103/PhysRevB.47.558.

[15] G. Kresse, J. Furthmüller, Efficient iterative schemes for ab initio total-energy calculations using a plane-wave basis set, Phys. Rev. B. 54 (1996) 11169–11186. doi:10.1103/PhysRevB.54.11169.

[16] H. Yamane, T. Yamada, Effects of stacking fault on the diffraction intensities of β-$FeSi_2$, J. Alloys Compd. 476 (2009) 282–287. doi:10.1016/j.jallcom.2008.08.078.

[17] C.A. Dimitriadis, J.H. Werner, S. Logothetidis, M. Stutzmann, J. Weber, R. Nesper, Electronic properties of semiconducting $FeSi_2$ films, J. Appl. Phys. 68 (1990) 1726. doi:10.1063/1.346601.

[18] H. Fujiwara, Y. Toyoshima, M. Kondo, A. Matsuda, Interface-layer formation mechanism in a-Si : H thin-film growth studied by real-time spectroscopic ellipsometry and infrared spectroscopy, Phys. Rev. B. 60 (1999) 13598–13604. doi:DOI 10.1103/PhysRevB.60.13598.

[19] I.A. Tarasov, N.N. Kosyrev, S.N. Varnakov, S.G. Ovchinnikov, S.M. Zharkov, V.A. Shvets, et al., Quick ellipsometric technique for determining the thicknesses and optical constant profiles of Fe/SiO_2/Si(100) nanostructures during growth, Tech. Phys. 57 (2012) 1225–1229. doi:10.1134/S1063784212090241.

[20] D. Barton, F.K. Urban, Ellipsometer analysis in the n–k plane, Thin Solid Films. 516 (2007) 119–127. doi:10.1016/j.tsf.2007.06.080.

[21] V. V Balashev, V. V Korobtsov, T.A. Pisarenko, E.A. Chusovitin, K.N. Galkin, Study of ultrathin iron silicide films grown by solid phase epitaxy on the Si(001) surface, Phys. Solid State. 52 (2010) 397–403. doi:10.1134/S1063783410020289.

[22] V. V. Balashev, V. V. Korobtsov, T. a. Pisarenko, E. a. Chusovitin, Influence of defects in a silicon dioxide thin layer on the processes of silicidation in the Fe/SiO_2/Si(001) system, Phys. Solid State. 51 (2009) 601–607. doi:10.1134/S1063783409030287.

[23] I.A. Tarasov, I.A. Yakovlev, M.S. Molokeev, M.. Rautskii, I.V. Nemtsev, S.N. Varnakov, et al., Growth of α-$FeSi_2$ nanocrystals on si(100) with Au catalyst, Mater. Lett. 168 (2016) 90–94. doi:10.1016/j.matlet.2016.01.033.

[24] C.A. Dimitriadis, J.H. Werner, Growth mechanism and morphology of semiconducting $FeSi_2$ films, J. Appl. Phys. 68 (1990) 93. doi:10.1063/1.347159.

[25] M.-A. Nicolet, S.S. Lau, Formation and Characterization of Transition-Metal Silicides, in: 1983: pp. 329–464. doi:10.1016/B978-0-12-234106-9.50011-8.

[26] J.A. Venables, Nucleation calculations in a pair-binding model, Phys. Rev. B. 36 (1987) 4153–4162. doi:10.1103/PhysRevB.36.4153.

[27] a. Wohllebe, B. Holländer, S. Mesters, C. Dieker, G. Crecelius, W. Michelsen, et al., Surface diffusion of Fe and island growth of $FeSi_2$ on Si(111) surfaces, Thin Solid Films. 287 (1996) 93–100. doi:10.1016/S0040-6090(96)08733-0.

[28] G. Madras, B.J. McCoy, Ostwald ripening in two dimensions: Time dependence of size distributions for thin-film islands, Phys. Chem. Chem. Phys. 5 (2003) 5459. doi:10.1039/b312257c.

[29] A. González-González, C. Polop, E. Vasco, Slope selection-driven Ostwald ripening in ZnO thin film growth, Phys. Rev. B. 86 (2012) 45434. doi:10.1103/PhysRevB.86.045434.

[30] Y. Terai, H. Yamaguchi, H. Tsukamoto, T. Hattori, T. Higashi, Effects of lattice deformations on Raman spectra in β-$FeSi_2$ epitaxial films, in: Proc. Int. Conf. Summer Sch. Adv. Silicide Technol. 2014, Japan Society of Applied Physics, 2015: p. 11109. doi:10.7567/JJAPCP.3.011109.

[31] R. Lang, L. Amaral, E.A. Meneses, Indirect optical absorption and origin of the emission from β-$FeSi_2$ nanoparticles: Bound exciton (0.809 eV) and band to acceptor impurity (0.795 eV) transitions, J. Appl. Phys. 107 (2010) 103508. doi:10.1063/1.3391977.

[32] Y. Maeda, H. Udono, Y. Terai, Raman spectra for β-$FeSi_2$ bulk crystals, Thin Solid Films. 461 (2004) 165–170. doi:10.1016/j.tsf.2004.02.059.

[33] H. Kakemoto, Y. Makita, S. Sakuragi, T. Tsukamoto, Synthesis and Properties of Semiconducting Iron Disilicide β-FeSi2, Jpn. J. Appl. Phys. 38 (1999) 5192–5199. doi:10.1143/JJAP.38.5192.

[34] F. Li, N. Lustig, P. Klosowski, J.S. Lannin, Disorder-induced Raman scattering in $NiSi_2$, Phys. Rev. B. 41 (1990) 10210–10213. doi:10.1103/PhysRevB.41.10210.

[35] D.Z. Chi, Semiconducting β-phase $FeSi_2$ for light emitting diode applications: Recent developments, challenges, and solutions, Thin Solid Films. 537 (2013) 1–22. doi:10.1016/j.tsf.2013.04.020.

[36] J.N. Hilfiker, N. Singh, T. Tiwald, D. Convey, S.M. Smith, J.H. Baker, et al., Survey of methods to characterize thin absorbing films with Spectroscopic Ellipsometry, Thin Solid Films. 516 (2008) 7979–7989. doi:10.1016/j.tsf.2008.04.060.

[37] J. Karel, J. Juraszek, J. Minar, C. Bordel, K.H. Stone, Y.N. Zhang, et al., Effect of chemical order on the magnetic and electronic properties of epitaxial off-stoichiometry Fe_xSi_{1-x} thin films, Phys. Rev. B. 91 (2015) 144402. doi:10.1103/PhysRevB.91.144402.

[38] H.-J. Kim, M. Sasaki, A. Ohnishi, M. Kitaura, M. Saito, S. Nonoyama, et al., Nature of magnetic impurity induced superparamagnetism and anomalous Hall effect in β-$FeSi_2$ single crystals, Phys. B Condens. Matter. 407 (2012) 126–130. doi:10.1016/j.physb.2011.10.001.

[39] G. Cao, D.J. Singh, X.-G. Zhang, G. Samolyuk, L. Qiao, C. Parish, et al., Ferromagnetism and Nonmetallic Transport of Thin-Film α−$FeSi_2$: A Stabilized Metastable Material, Phys. Rev. Lett. 114 (2015) 147202. doi:10.1103/PhysRevLett.114.147202.